Using PWM-Induced Transient Excitation and Advanced Signal Processing for Zero-Speed Sensorless Control of AC Machines

Markus A. Vogelsberger, Stefan Grubic, *Student Member, IEEE*,
Thomas G. Habetler, *Fellow, IEEE*, and Thomas M. Wolbank, *Member, IEEE*

***Abstract*—The sensorless control of induction machines, particularly for operation at low speed, has received significant attention in recent years. To realize a field-oriented control of ac machines that is able to work at zero speed, the most commonly used methods are either sensor-based models or transient-signal-excitation methods. The major disadvantage of present signal-injection methods is that they are intrusive to pulsewidth modulation (PWM). An additional switching sequence has to be embedded in the control that will cause a torque and current ripple. In order to overcome these problems, a new flux-estimation algorithm that uses the phase current derivative to extract the flux-position information is presented. In contrast to previously introduced methods, this new approach operates without additional transient excitation of the machine and requires only fundamental-wave excitation using standard PWM or slightly modified PWM. Furthermore, only the current response in the two active states of PWM is used. This makes it possible to use sensorless control for the whole speed range including overmodulation and removes the distortion and parasitic influence of the zero switching states during the estimation of the flux. Experimental results are presented to validate the applicability of the presented approach.**

***Index Terms*—AC motor drives, current measurement, induction motor, neuronal networks, pulsewidth modulation (PWM), saturation, speed control, transient response.**

I. Introduction

INDUCTION machines are widely used in industrial applications involving electromechanical energy conversion due to their favorable attributes like low cost, reasonable size, robustness, and low maintenance. Many of these applications require the use of adjustable-speed drives and a suitable control system that provides a large operating range and good dynamic performance. The most commonly used techniques are field-oriented and direct torque controls. The implementation of both control algorithms requires the identification of the flux angle in order to perform the required switching transitions of the inverter.

Manuscript received December 19, 2008; revised July 28, 2009. First published August 21, 2009; current version published December 11, 2009. This work was supported by the Austrian Science Fund (Fonds zur Förderung der wissenschaftlichen Forschung) under Grant P19967-N14.

M. A. Vogelsberger and T. M. Wolbank are with the Department of Electrical Drives and Machines, Vienna University of Technology, 1040 Vienna, Austria (e-mail: markus.vogelsberger@tuwien.ac.at; thomas.wolbank@tuwien.ac.at).

S. Grubic and T. G. Habetler are with the School of Electrical and Computer Engineering, Georgia Institute of Technology, Atlanta, GA 30332-0250 USA (e-mail: sgrubic@ece.gatech.edu; thabetler@ece.gatech.edu).

Digital Object Identifier 10.1109/TIE.2009.2029578

Currently, all highly dynamic ac drives are equipped with a mechanical shaft sensor in order to estimate the necessary flux position for field-oriented control. Omitting this sensor has several advantages and has therefore been a topic of high interest in recent years. Some advantages of sensorless control are the reduction of the hardware complexity, lower costs, increased reliability, and less maintenance requirements.

Using fundamental-wave models with accurate sensors for voltage and current, speed sensorless operation of induction machines is possible down to slip frequency, corresponding to mechanical standstill. However, at zero frequency, these models fail, and stable sensorless operation is considered to be only possible by applying the so-called signal-injection methods.

By injecting a high frequency or transient signal in addition to the fundamental wave, saliencies caused by spatial saturation, slotting, and anisotropy can be extracted and exploited to directly estimate the flux position. These signal-injection methods usually inject a voltage excitation and measure the current reaction of the machine. Present signal-injection-based methods rely on the additional high frequency or transient signal excitation of the machine. The excitation can either be realized in a harmonic sense as a pulsating or rotating component or in a transient sense as a sequence of voltage pulses, as explained in the literature.

By using a high-frequency (several hundreds of hertz up to kilohertz) voltage-injection method with a rotating [7], [8], [24], [25] or a pulsating vector [9], the measured HF current reaction can be demodulated and processed to extract the position information. When using these methods, special care has to be taken to overcome the effect of the inverter interlock deadtime, which causes a disturbance every 60°—also called current clamping in the literature—as well as other side effects, including those caused by the current control loop.

Transient-signal-excitation approaches [10], [18], [19] or methods exploiting transient voltage changes within the space-vector pulsewidth modulation (PWM) [1], [2], [5] use the machine current reaction to determine the saliency information, which is the basic principle for sensorless control.

This paper presents first a method to detect the flux angle using an additional transient test voltage injected into the machine. Then, this method is then extended such that the excitation of the machine and, thus, the flux-angle measurement are performed only based on the fundamental-wave excitation of the machine without injecting additional test voltages.

The concept is introduced, and its applicability is validated by experimental results.

II. Position Estimation—Sensorless Control Without Signal Injection

A fundamental component of the flux-angle estimation is the exploitation of spatial main-flux saturation by means of the current-derivative or current-slope measurement. In recent years, several new signal-injection-based approaches that integrate the di/dt measurements within the fundamental space-vector PWM (SVPWM) sequence have been presented [1]–[6], [18], [19]. In theses methods, all three inverter states of a PWM cycle (two active plus the inactive state) are used to exploit the saliency information. To avoid the parasitic effects of the inactive switching state, particularly near zero frequency, only the two active states are used for evaluation in the proposed method.

To guarantee a minimum pulse duration, which is necessary for a current-slope measurement in [1], [5], [18], and [19], SVPWM is modified by introducing additional compensating switching states with inverse direction. In [5], PWM is modified using nonadjacent voltage vectors but switching states with a spatial angle difference of 120°. The new approach introduced in this paper does not require the modification of SVPWM. Only a slight modification of the current controller has to be implemented. This is an advantage with respect to practical implementation since the values of the duty cycles within SVPWM need not be modified. In addition, the flux-estimation algorithm is also simpler since the available output voltage vector from the current controller can directly be used. In order to provide some insight on the new noninvasive method, a similar approach that uses an additional signal injection is first introduced and validated by experiment. Subsequently, the noninvasive method is presented.

A. Fundamentals and Standard PWM Injection

The basic idea of the injection method is to extract a signal that is correlated to the transient leakage inductance of the machine. Since the leakage inductance is affected by the inherent saliencies, the modulation of this correlated signal can be exploited to estimate the spatial positions of the saliencies.

The correlated signal used for the flux-angle estimation is the derivative of the current resulting from a voltage-pulse excitation. This current derivative with respect to time will also be denoted as current slope in the following.

For a symmetrical machine (without inherent saliencies), the relation between the stator voltage and the resulting change in current is represented by the stator voltage

$$\underline{u}_S = r_S \cdot \underline{i}_S + l_\sigma \cdot \frac{d\underline{i}_S}{d\tau} + \frac{d\underline{\lambda}_R}{d\tau}. \tag{1}$$

The time derivative of the current $d\underline{i}_S/d\tau$ depends on the applied voltage $\underline{u}_S$, the back electromotive force (EMF), the stator-resistance voltage drop, $r_S \cdot i_S$, as well as the value of leakage inductance l_σ. The stator resistance and the back EMF act as disturbances for the identification of leakage inductance and therefore have to be eliminated. By applying two voltage vectors pointing in different spatial directions and measuring the resulting current time derivative, two sets of stator equation are obtained. The elimination of disturbances can then be performed by subtracting the two equations. In order to perform the elimination of disturbances, difference voltage vectors and difference current-slope vectors can be defined, as will be explained later. These difference vectors automatically take care of the disturbance elimination.

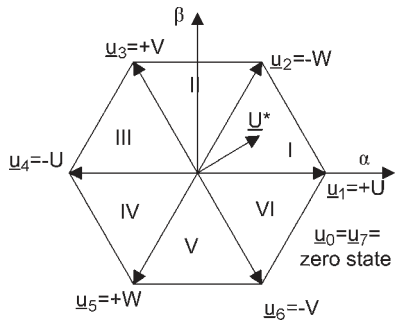

Fig. 1. Definition of the voltage space vectors and PWM sectors.

The inherent saliencies of the machine affect the symmetry of the three transient phase leakage inductances, leading to a complex value of leakage $\underline{l}_\sigma$

$$\frac{d\underline{i}_S}{d\tau} = \underline{u}_S \cdot \frac{1}{\underline{l}_\sigma}. \tag{2}$$

By measuring the transient current response, it is therefore possible to detect and locate the spatial positions of the saliencies.

In SVPWM, the value of a reference voltage vector is adjusted by applying two active "neighboring" switching states and the two zero switching states during each PWM cycle. The complex space-vector plane where those vectors are lying in is shown in Fig. 1.

The basic vectors labeled with $\underline{u}_i$ are used to generate the desired output voltage. They span the PWM sectors labeled with "I"–"VI."

Since SVPWM is using two voltage vectors pointing in different spatial directions during each PWM cycle, it is theoretically always performing a voltage-pulse sequence that is suitable for eliminating the disturbances of stator resistance and back EMF.

Considering the operation of SVPWM and the sequence of the voltage vectors, one can define difference voltage vectors. The difference voltage vectors can be calculated directly based on the sector of the reference voltage and the switching sequence. They are denoted as $\underline{u}_{12}$, $\underline{u}_{23}$, and $\underline{u}_{31}$ and are defined according to (3), with the subscript number indicating the position within the switching sequence running from 0 (first zero state) to 3 (second zero state)

$$\underline{u}_{ij} = \underline{u}_i - \underline{u}_j. \tag{3}$$

To determine the time derivative of the current, two different methods can be applied (Fig. 2). One option is to perform at least two measurements at two different time instants and to approximate the time derivative by the differential quotient (4).

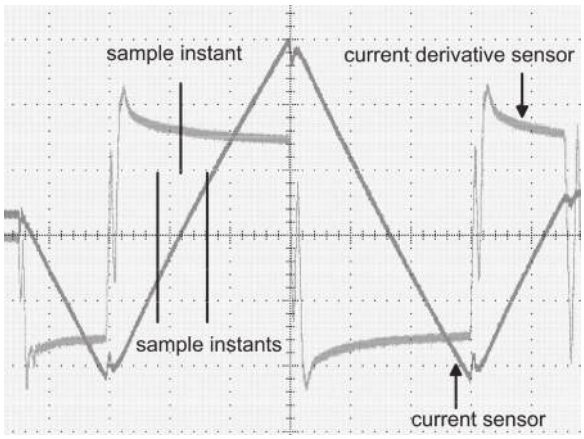

Fig. 2. Measurement of the current-slope vector using a current sensor and a current-derivative sensor.

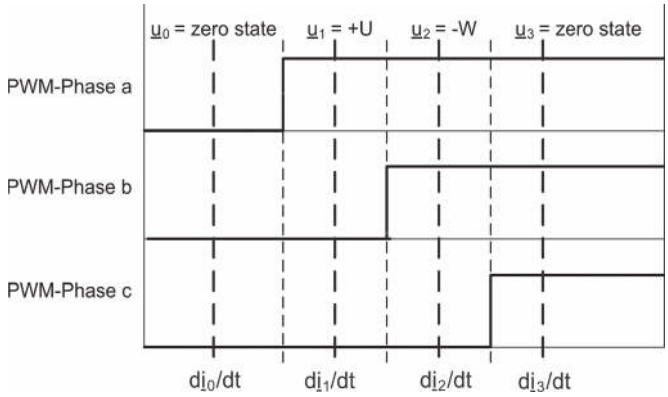

Fig. 3. Current-slope sampling during the pulse sequence initiated by SVPWM (reference voltage vector $\underline{u}^*$ according to Fig. 1).

The other is to apply a sensor current derivative inspector (CDI) whose output is directly correlated to the time derivative [13]. This CDI sensor only needs one sample to determine the current derivative

$$\frac{\partial i}{\partial t} \approx \frac{\Delta i}{\Delta t} = \frac{i(t+\Delta t)}{\Delta t} - \frac{i(t)}{\Delta t}. \tag{4}$$

Fig. 2 shows the two methods for the measurement of the current slope.

In Fig. 3, the fundamental SVPWM sequence for a voltage vector $\underline{u}^*$, like that depicted in Fig. 1, is shown.

This figure also shows the time instants at which the current-slope samples are taken.

One can then define the difference current-slope vector, $d\underline{i}_{ij}/dt$, according to (5) from the current-slope vector ($d\underline{i}_1/dt$, $d\underline{i}_2/dt$, and $d\underline{i}_3/dt$). The evaluation algorithm, which determines the flux angle, uses only the difference current-slope vector, $d\underline{i}_{12}/dt$, from the two active states. That is

$$d\underline{i}_{12}/dt = d\underline{i}_1/dt - d\underline{i}_2/dt. \tag{5}$$

Fig. 4 shows the measured trajectories of the three possible difference current-slope vectors for the SVPWM voltage-vector area "V" $(+W/-V/0)$. The machine was operated at rated flux and a torque-producing current component that was equal to 0.7 p.u.

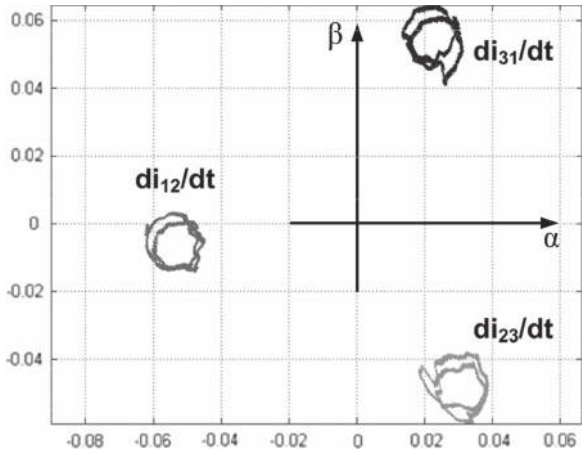

Fig. 4. Locus of the three differential current-slope vectors corresponding to the voltage-space-vector area "V" $(+W/-V/0)$ (rated flux, torque current $= 0.7$ p.u.).

The three switching states are $\underline{u}_1 = +W$, $\underline{u}_2 = -V$, and the zero state $\underline{u}_3 = 0$. The black trace denoted as $d\underline{i}_{12}/dt$ in Fig. 4 represents the trajectory for $d\underline{i}_{12}/dt$ that is obtained for current-slope measurements during active states $+W$ and $-V$.

The two traces, namely, $d\underline{i}_{23}/dt$ and $d\underline{i}_{31}/dt$, respectively, are obtained for one active switching state ($+W$ or $-V$) and the zero switching state. When comparing the three traces in Fig. 4, it can be seen that the trajectory for $d\underline{i}_{12}/dt$ has the lowest distortion. When measuring the current derivative during a zero voltage vector, the signal magnitude is very low, leading to an increased sensitivity to noise in the analog-signal path. In addition to this low signal level, there is also a disturbing effect of the nonideal inverter properties. Since the voltage drops of transistor and diode are unequal, their influence is superposed on the modulation of the saliencies and therefore acts as a disturbance.

The basic principle of integrating fundamental-wave excitation and transient excitation is not completely new [1], [3], [4]. However, in [1], [3], and [4] all three switching states (two active states and the zero vector) are exploited for the detection of the saliencies.

The use of only the active switching states is proposed in this paper and has two main advantages. First, the distortion introduced by the zero-switching-state measurements can be avoided. Second, including the zero switching state in the measurements and evaluation limits the method when the sensorless position control has to be established for the whole speed range including overmodulation.

Another method of integration was proposed in [5]. In that paper, the standard SVPWM method is modified by extending the 60° voltage sector to a 120° sector and thus does not use the two adjacent switching states. This results in increased current ripple. In case that one of the switching states is too short to measure, a sequence of six switching states is proposed containing two zero states and four active voltage vectors. The four active vectors are a combination of two adjacent ones, followed by a zero vector and another pair of adjacent vectors pointing in the opposite direction of the first one. The

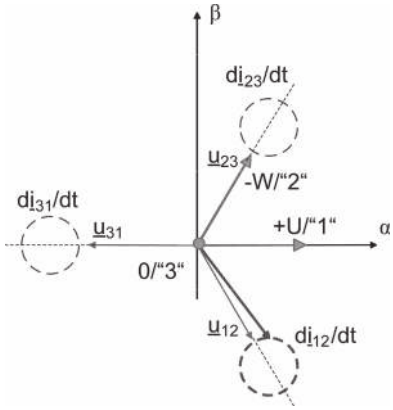

Fig. 5. Trajectories of the difference voltage vector and the difference current-slope vector for the specified SVPWM sector.

measurements of the six switching states are finally combined into one saliency measurement.

From previous research, it is well known that the ratio of the difference current-slope vector $d\underline{i}_{12}/dt$ and the corresponding difference voltage vector $\underline{u}_{12}$ is correlated to the inherent saliencies. In the case of a machine with closed rotor slots, the dominant saliency is caused by spatial saturation. Thus, the aforementioned correlation is dominated by the $+2$nd-harmonic frequency caused by main-flux saturation.

In Fig. 5, the difference voltage space vectors and the difference current-slope space vectors for an excitation voltage that is lying in sector "I" $(+U/-W/0)$, which is equivalent to states $\underline{u}_1 = +U$ (1st active state), $\underline{u}_2 = -W$ (2nd active state), and $\underline{u}_3 = 0$ (2nd zero state), are shown.

In a first step toward the integration of the pulse sequence into SVPWM, the difference current-slope vector $d\underline{i}_{12}/dt$ and, thus, the saturation angle as an approximation of the flux position have to be determined by a periodic injection of one specific reference voltage vector (test-pulse sequence). For example, the reference voltage vector $\underline{u}^*$, as shown in Fig. 1, which lies in sector "I" $(+U/-W/0)$ and has a phase angle of $+30°$, is used to identify $d\underline{i}_{12}/dt$, which is independent of the direction of the fundamental wave.

Applying the algorithms described earlier, the resulting signals can be depicted in the complex plane, as shown in Fig. 5. Assuming a sinusoidal modulation of leakage inductance, the trajectories of the difference current-slope vectors lead to the dashed circles. Depending on the switching states during which the current slope is evaluated, the center of the individual circles is shifted. With the measurement sequence being assumed earlier $(+U/-W/0)$, the circle marked $d\underline{i}_{12}/dt$ is obtained for the active states.

Instead of only injecting the test-voltage sequence into sector "I," the difference current-slope trajectories are also investigated if the injected voltage lies in sectors "II"–"VI." Again, only the active states and, thus, $d\underline{i}_{12}/dt$ are used for evaluation. This leads to six different traces for $d\underline{i}_{12}/dt$. The measurement results are shown in Fig. 6 and are taken at a load current of 0.2 p.u. The voltage vector injected into sector "I" ($\underline{u}^*$, solid black) and the corresponding difference current-slope vector labeled with I (black, denoted as $d\underline{i}_{12}/dt$) show the modulation caused by the inherent saliencies. The results for reference

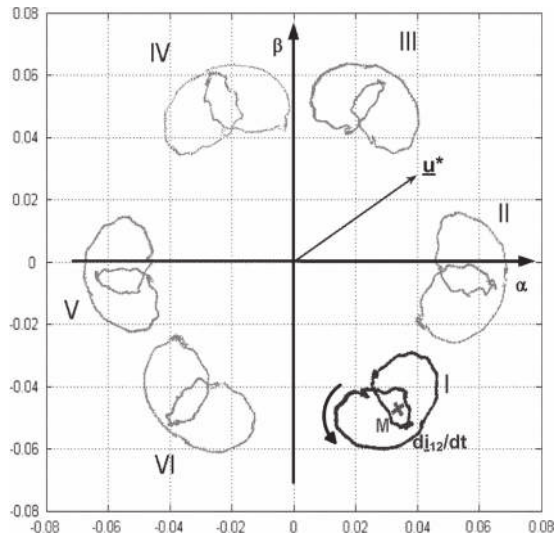

Fig. 6. Trajectories of the difference current-slope vector $d\underline{i}_{12}/dt$ for reference voltages in all six sectors (load current $= 0.2$ p.u.).

voltages lying in the other SVPWM sectors (gray, "II"–"VI") are labeled equivalently.

The dominant $+2$nd harmonic in the current-slope vectors induced by spatial main-flux saturation can clearly be identified from Fig. 6. For one electrical revolution, the difference current-slope vector $d\underline{i}_{12}/dt$ makes two full rotations. The distortion of the circle is due to the presence of additional harmonics.

B. Exploitation of the Fundamental-Wave PWM Excitation

The method of Fig. 6 is considered to be invasive to SVPWM since an additional voltage vector has to be injected. Furthermore, the injected voltage sequence will increase the current and torque ripple. Thus, it is desirable to find a way to determine the differential current-slope vector without changing or modifying the SVPWM algorithm.

In a final step, the difference current-slope vector is obtained using only difference current-slope samples taken during the pulse sequences created by SVPWM, with the reference values being generated by the fundamental-wave current controller. In order to simplify the discussion, only steady-state operation of the machine is considered.

The output of the current controller, which is the same as the reference voltage, is moving along the six voltage-space-vector areas ("I"–"VI"). This reference vector may thus be interpreted as a moving test-pulse sequence/excitation. If the reference voltage is lying very close to the border of one of the sectors, there is too little time for an accurate current-slope measurement [1], [2]. In these cases, the current controller can be modified for a single PWM cycle such that these areas are avoided. This corresponds to introducing a dead zone without any modification of the current-controller structure. The proposed approach requires only one PWM period to successfully estimate the saturation angle and, out of it, the flux position. The aforementioned modification for only a single PWM cycle is thus sufficient.

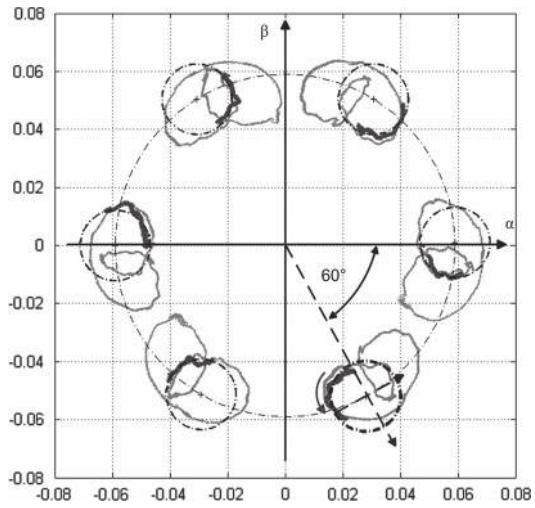

Fig. 7. Trajectories of the difference current-slope vector for the fundamental-wave PWM (load current $= 0.2$ p.u.).

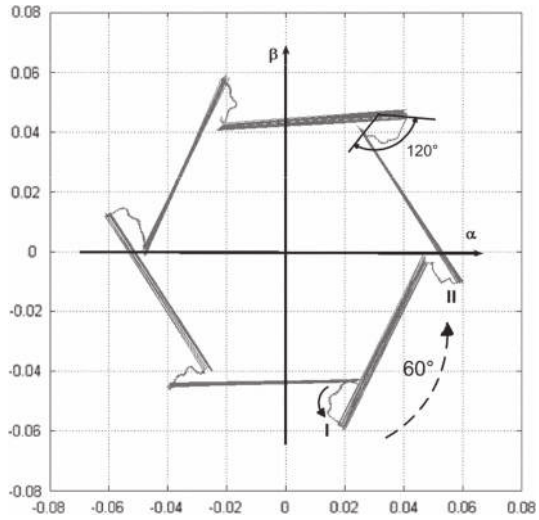

Fig. 8. Locus of the difference current-slope vector obtained from the excitation sequences integrated into SVPWM (load current $= 0.2$ p.u.) for two fundamental-wave periods.

If the fundamental current control requests a fundamental voltage that lies close to an active vector for a longer period, it is not necessary to always modify the current-controller output. For example in the case of zero fundamental frequency and steady-state operation, it is adequate to reduce the sampling frequency for the flux position involved with the modification.

This concept does not require the injection of an additional voltage, and therefore, SVPWM remains unchanged. Merely the control algorithm has to be modified slightly.

The actual voltage feeding the machine would stay the same in both versions (current-regulator or SVPWM level). However, SVPWM is usually realized in hardware (counter/capture/compare), which requires additional calculation of the modified duty cycles. The dead-zone approach in the current-controller level can thus be implemented with more simplicity at a lower cost.

Since the difference current-slope trajectory is not obtained for a voltage that is only injected into one sector, there will not be a closed-loop trajectory for the difference current slope, as shown in Fig. 6. Instead, the trajectories shown in Fig. 7 (black) are obtained, which are generated by using the current-controller output voltage as the injected test/reference voltage. As shown in Fig. 7, for each voltage sector, only a 120° section (thick, black) of each of the difference current-slope trajectories (thin, gray—similar to the ones shown in Fig. 6) is obtained.

The reference voltage vector no longer has a fixed angle due to the rotating current-controller output voltage that is now used as excitation. Therefore, the thick black segments of difference current-slope trajectories are not exactly the same as the ones shown in Fig. 5 but very similar in shape and location.

The frequency of the difference current-slope trajectory caused by spatial main-flux saturation is twice (+2nd harmonic) as big as the fundamental voltage.

Therefore, the differential current slope makes two revolutions for one electrical revolution of the reference voltage vector. Thus, the rotational angle of the difference current-slope trajectory is equivalent to 120°, while the reference voltage vector covers a sector of 60°.

Each time the reference voltage vector crosses over to the next sector area, the center of the differential current-slope trajectory jumps/rotates by 60°, which is described by the straight lines (gray) in Fig. 8 that connect the 120° segments. For each SVPWM sector area (each 60°), there will be a 120° section of a circle such that the overall rotation of the difference current slope during one electrical revolution of the fundamental wave is $6 \cdot 120° = 2 \cdot 360°$. In Fig. 8, the 120° segments of the differential current-slope trajectory corresponding to the first and second SVPWM sectors are labeled with "I" and "II."

The key signal for speed sensorless control is the angular position of the saliency. In order to extract the angle information from the differential current-slope trajectory segments, the centers of the trajectory segments have to be determined. This can be done in one of two ways.

One way to determine the centers of the different segments is based on geometrical considerations. Since each of the difference current-slope trajectories describes a 120° segment of a circle, it is possible to determine the center of rotation for each of the sections. All centers are spatially located on a circle each lying 60° apart, as shown in Fig. 7. In addition, a reference coordinate system can be defined at the center of each identified circle whose real axis corresponds to the direction of the difference voltage vector. This coordinate system is shown for SVPWM sector "I" in Fig. 7 (dashed). Similar coordinate systems are defined at the centers of the other 120° segments. This leads in a final step to the situation wherein all coordinate systems and, therefore, all trace segments (120° segments) are lying on top of each other.

The other method is to divide each of the difference current-slope traces by the corresponding difference voltage vectors according to (2). The trace segments (120° segments) resulting from this equation are lying on top of each other at the positive real axes of the stator-fixed reference frame (α-axis), such as that shown in Fig. 9. In a second step, the center (M) for each of these six 120° segments has to be estimated. For the estimation of the centers, all measurements are performed at steady-state

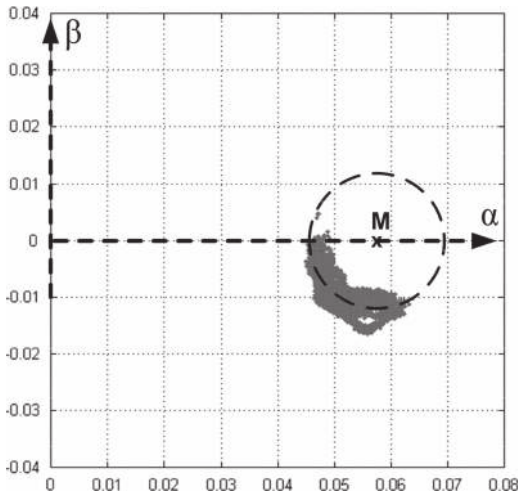

Fig. 9. Locus of the difference current-slope vector (120° segments) after division with the corresponding difference voltage vector.

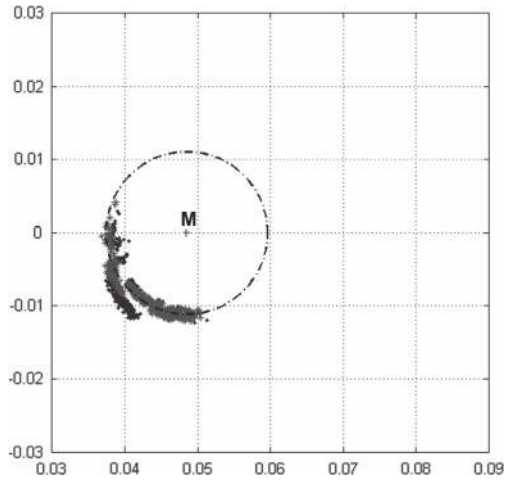

Fig. 10. Circle-center determination by using the RANSAC algorithm. (Light gray) All measurement points. Used data points by (dark gray) RANSAC to determine the center.

operation to ensure equal 120° sectors. Once the positions of the centers are known, this limitation is no longer necessary.

Common techniques for such a location-determination problem (e.g., circle approximation), such as the least squares algorithm, use all of the presented/existing data to solve the problem and have no mechanism to detect and sort out error data points from the measurement. For this specific application, an alternative method has been used, which gives a better result. The method is described hereinafter.

A better method to solve the location-determination problem (circle approximation/center of a circle segment determination) is the random sample consensus (RANSAC) algorithm [22]. In contrast to the least squares method, RANSAC is much more suitable for use in automatic solving, fitting, and location-determination problems applied to measured data points. This is based on the fact that RANSAC is using only a few initial data points from the whole data stream at the beginning and sequentially enlarges the data set with consistent values later in progress. Furthermore, RANSAC offers a mechanism to handle and reject error data points out of the whole stream and is thus using only reliable values for the fitting.

For the aforementioned problem of searching the circle center, the algorithm starts with three random measurement points to compute an implied center. In step 2, further measurement points are used to confirm the suggested solution. In the further steps, the compatibility of the implied solution is checked, and if compatibility is not reached, a new attempt starting with step 1 will be initiated. As shown in Fig. 10, RANSAC is able to determine the circle center from the scattered plot of the measurement points. Furthermore, it can be seen that RANSAC is using only "good points" (black) for the calculation and ignores the outliers (gray).

To minimize the influence of measurement errors, a combination of both methods described earlier has been applied in this paper. The identification of the center of the different 120° segments has to be done once online during a commissioning period before the sensorless operation.

After applying the method described previously, all coordinate systems have the same center, with all real and imaginary

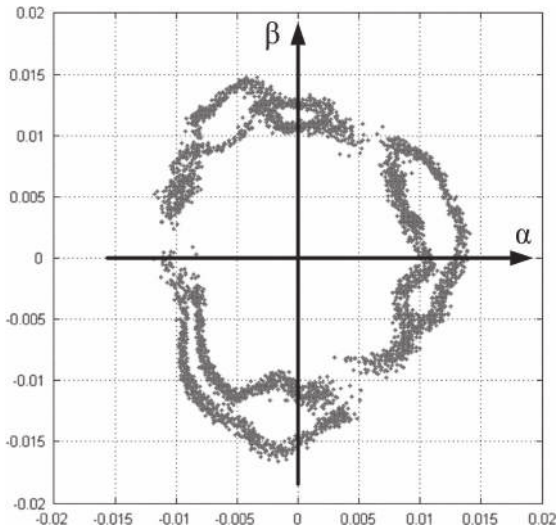

Fig. 11. Trajectories of the differential current-slop vector for two electrical revolutions.

axes being aligned. In this common reference system, all trace segments are lying on top of each other at angular positions from $-180°$ to $-60°$. This 120° segment is caused by the movement of the fundamental wave by 60° within the corresponding sector, as already mentioned.

The angular position of the individual traces must be accurately separated. Each trace has to be transformed within the reference coordinate system by the angle of the corresponding difference voltage vector, multiplied by the harmonic number of the saliency (with respect to the fundamental wave). In the case of saturation saliency, the transformation angle is a multiple of $120° \ (2 \cdot 60°)$.

The application of this transformation to each of the six sector traces leads to a closed-loop trajectory representation, which can now be used to extract the required angle information. The result of this process is shown in Fig. 11 for one revolution of the fundamental wave. The former six separate trajectories now form a continuous curve that shows two rotations around the origin. Thus, the dominant $+2$nd harmonic that is characteristic

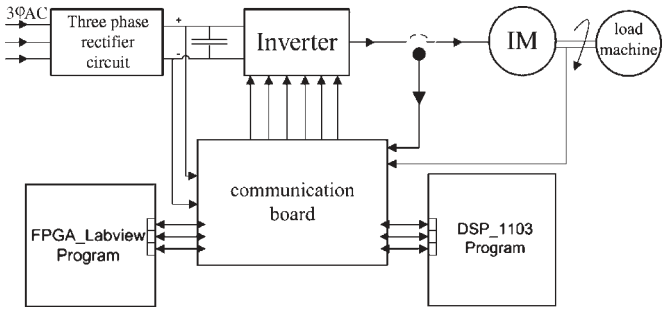

Fig. 12. Block diagram of the measurement setup.

for the differential current slope caused by spatial main-flux saturation can clearly be seen. This harmonic can then be used to determine the sensorless estimated saturation angle, which is used for sensorless control.

There is, however, a phase shift between the saturation angle and the rotor-flux angle, which shows a strong dependence on the flux and/or load level of the machine [21]. The compensation of flux/load dependence, as well as the higher harmonics due to the nonsinusoidal distribution of saturation along the air gap, is usually done in a separate step. In this paper, the compensation is done using a neural-network approach that is similar to that in [20].

The results presented in this paper were obtained from a closed-slot machine. This type of machine has one dominant saturation saliency that has heavy load dependence. The results are thus dependent on the machine. In the case of an unskewed open-slot machine, for example, automatic tracking and separation of different saliencies must be compensated. This separation, however, is usually done together with the compensation of flux/load dependence using a neural-network approach or similar techniques [26].

III. Measurement Results

To verify the applicability of the new method in a machine-driven environment, measurements have been carried out using an appropriate test bed. In Fig. 12, the test configuration is shown. It consists of a power converter, a control system with the communication board, an induction machine, and a load machine. The 11-kW closed-slot induction machine is fed by a inverter with field-oriented SVPWM control using a switching frequency of 5 kHz. The machine is coupled to the load dynamometer.

The control electronics consist of two main components. The first component consists of a signal-processor board (dSpace 1103) programmed in Matlab/Simulink and is responsible for all control tasks. The second component is a field-programmable gate array (FPGA) system and is responsible for the PWM generation, the sampling of the sensors, as well as some data preprocessing. The communication between both systems is realized using an interface board for the data transfer.

The control electronics consist of two main components. The first component consists of a signal-processor board (dSpace 1103) programmed in Matlab/Simulink and is responsible for all control tasks. The second component is an FPGA system and is responsible for the PWM generation, the sampling of the sensors, as well as some data preprocessing. The communication between both systems is realized using an interface board for the data transfer.

The real-time processing requirements can be compared to the methods in [1], [2], and [10]. In [10], pulse excitation is done separately from the modulation method, which results in a minimum performance needed. The only requirements are the pulse generation itself and the sampling at specific time instants. The number of necessary calculations is limited to a few additions and multiplications.

In [2], the PWM sequence has to be modified. As almost all of today's digital signal processors (DSPs) usually have a capture/compare unit, most of the necessary modifications can be carried out by built-in hardware. The mathematical burden is slightly increased compared to that in [10] as modification and sampling get more complex.

The methods proposed in this paper, as well as that in [1], have increased requirements. Not many details are given about this in [1] and [5]. However, it can be concluded that, as the excitation sequence changes with the fundamental-wave position, additional coordinate transformations have to be carried out using both methods. As the method proposed here uses a reduced number of samples, the real-time computation requirements are lower.

For the application of the method in an industrial environment, it is important to mention that the calculation of the RANSAC algorithm is limited to the commissioning phase and is thus not a burden for real-time processing. The estimation in this paper has been carried out in a combination of a DSP and an FPGA, as is frequently done in modern industrial drives. The increase in task time on the DSP was only a few percent when using the proposed method. Therefore, an integration of the proposed signal-processing structure using one single modern DSP is possible.

For the estimation, the overall signal-processing chain is carried out step by step, as described previously. First, the differential current-slope segments belonging to the active states of SVPWM are determined. Then, the center for each of the segments is calculated and transformed into one common coordinate system. Finally, the individual sector traces are transformed to obtain a resulting closed trace containing the results of all six sectors. Due to the design of the test machine (closed rotor slots), the modulation of the signal is dominated by the saturation saliency, leaving other saliency components negligible. Thus, the calculated angle gives the angular position of the saturation saliency, which contains the desired information of the rotor-flux angle used for sensorless control.

Existing phase offsets/shifts between the saturation angle and the rotor-flux angle (which show strong dependence on the flux/load level of the machine), as well as disturbing higher harmonics (due to the nonsinusoidal distribution of saturation along the air gap), must effectively be compensated to obtain the sensorless estimated rotor-flux angle. The application of the neural-network technique to machine control is proposed in [27]–[30]. In this paper, an artificial-neural-network (ANN) structure, which is similar to the approach in [20], is applied to compensate the aforementioned effects.

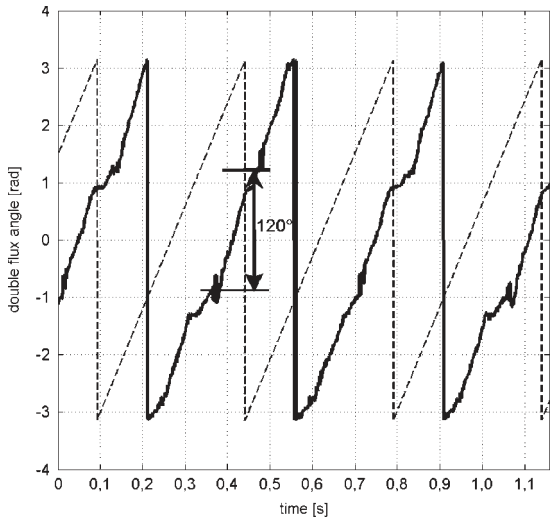

Fig. 13. Time traces of (thin gray) the reference twice flux angle and (solid black) the raw sensorless estimated saturation angle at mechanical standstill with a torque-producing current component $iy = 0.8$ p.u.

In Fig. 13, the measurement results of the signal-processing chain are shown. The machine has been operated at rated flux with a torque-producing current component of 0.8 p.u. at mechanical standstill.

The thin dashed gray trace represents twice the flux angle calculated from a sensor-based model as a reference. The estimated saturation angle is given in solid black.

This saturation angle is directly derived using the proposed estimation algorithm after combining the individual sector traces to one resulting signal. It is labeled as the "raw sensorless estimated saturation angle" in the figure and represents an internal signal that has to be further processed before using it for sensorless control. The points at which the voltage vector of SVPWM switches between adjacent sector areas can easily be identified in Fig. 13.

Several factors influence the quality of flux-angle estimation. One important issue is the determination of the centers of the individual traces of the differential current-slope vector trajectory for the different sectors of SVPWM. The positions of these centers are dependent on the mean transient inductance and thus move with the machine point of operation. An appropriate adjustment has thus to be included, as well as the compensation of load-dependent angle deviation using the ANN structure mentioned earlier.

All of the published transient-excitation methods are influenced by a change of the mean transient inductance and need to eliminate this effect. In [10], this is established by combining the results of three different excitation directions, which has the lowest complexity. In [1] and [5], this elimination is realized by combining two different active or a combination between active and inactive switching states, which slightly increases complexity. In [1] and [5], open-slot machines with clear dominating slotting saliency are used, wherein the influence of the mean inductance change is negligible compared to the position signal. The machine used in this paper, however, has closed rotor slots, and therefore, the inductance depends on the load. Thus, special measures were taken by combining the estimation algorithm with a neural-network approach.

Fig. 14 shows the sensorless controlled operation using the proposed excitation and signal-processing method. It has to be emphasized that, in order to show the performance of the method, the estimated angle is directly used to control the machine without any further fundamental-wave model of the machine.

The steady-state and transient performance of the proposed structure at zero mechanical speed during a torque step is shown in Fig. 14. A torque step is applied to the test machine that is driving a speed-controlled load machine. At the time instant $t = 3.1$ s, the reference step for the torque is applied (torque-producing current component from 0.2 to 0.8 p.u.). The time instant of the load step is marked with a cursor.

In the upper plot of Fig. 14, the solid thick black trace represents the time trace of the flux angle obtained from the transient current response, which is corrected by the neural network. The thin dashed trace gives the flux angle calculated with a sensor-based model as a reference. The middle plot of Fig. 14 shows the angle deviation between the sensorless estimated flux angle and the flux angle calculated using a sensor-based model as a reference. The deviation of the flux angle stays within ± 0.05 rad corresponding to $\pm 2.8^\circ$ during the whole experiment. A periodic change in angle deviation is observable, which stems from the crossover of the fundamental-wave voltage from one sector to the next.

The lower part of Fig. 14 shows the load current/torque step.

The proposed new flux-evaluation approach and the control structure are able to guarantee stable operation at zero mechanical speed during transient operation.

The performance of the sensorless controlled operation from the overall structure, using the proposed excitation and signal-processing method, with an operating point near zero electrical frequency is shown in Fig. 15. In this case, the machine was operated with a constant torque-producing current component of 0.6 p.u., with the speed-controlled load dynamometer being coupled to the motor under test.

Fig. 15 shows the time trace of the sensorless obtained flux angle, which is corrected by the neural network. At the left side of the figure, slow clockwise electrical rotation of the flux was chosen. In the center of the figure, the operation was changed to zero flux frequency for around 4 s, and on the right side, counterclockwise flux rotation is shown.

The stable behavior of the sensorless controlled drive at critical operation (changing the direction of flux rotation from slow clockwise electrical rotation to flux standstill and then to counterclockwise rotation) shows the effectiveness of the proposed new flux-evaluation approach.

IV. Conclusion

A method to integrate the transient excitation necessary for speed sensorless control into the fundamental-wave vector PWM has been presented, as well as the required signal processing to obtain the angular position of the saturation saliency. The signal processing is based on defining new reference frames for each excitation and on a combined mathematical and geometrical estimation of the origin of each of the reference frames.

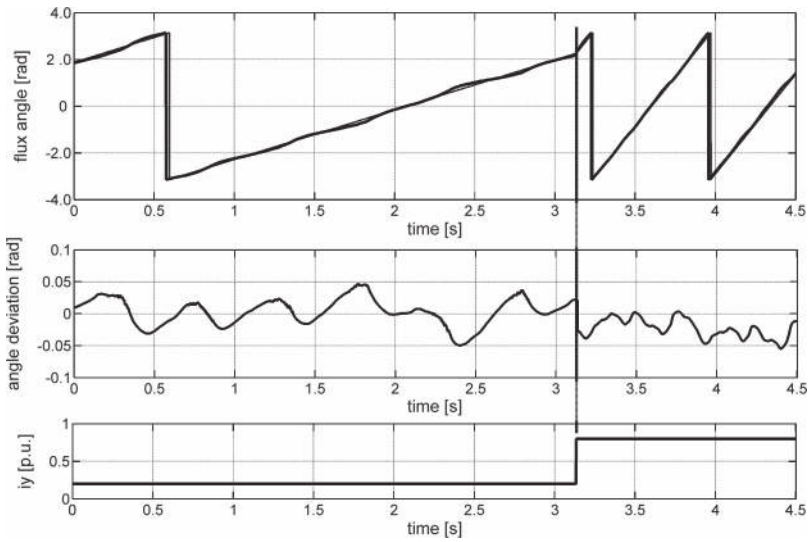

Fig. 14. Measurement results of sensorless controlled operation at mechanical standstill—step of the torque-producing current component from 0.2 to 0.8 p.u. (Upper) (solid, thick, black) Flux angle sensorless; (thin, dashed, black) sensor based. (Middle) Angle deviation (in radians). (Lower) Step of the torque-producing current component.

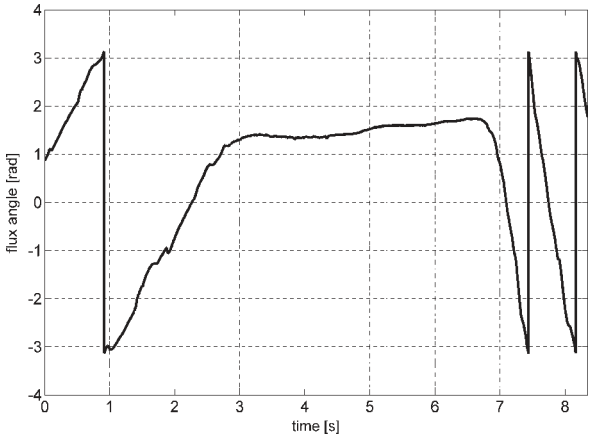

Fig. 15. Measurement result of flux angle at sensorless controlled operation at low/zero electrical frequency. (Left) Positive flux rotation. (Middle) Flux standstill. (Right) Negative flux rotation.

Combining the results of the different excitation sectors, a closed trace of the saliency modulation has been obtained, which can be evaluated to determine the saliency position necessary for speed sensorless control.

For the measurements, the sampling of the difference current-slope vector is done only during the active inverter switching states to reduce the disturbing influences of the inverter. The measurement results verify good steady-state and transient properties using this type of excitation/signal processing.

REFERENCES

[1] Q. Gao, G. M. Asher, M. Sumner, and P. Makys, "Position estimation of AC machines over a wide frequency range based on space vector PWM excitation," *IEEE Trans. Ind. Appl.*, vol. 43, no. 4, pp. 1001–1011, Jul./Aug. 2007.

[2] T. Wolbank and J. Machl, "A modified PWM scheme in order to obtain spatial information of AC machines without mechanical sensor," in *Proc. IEEE APEC*, 2002, pp. 310–315.

[3] P. Weinmeier, "Sensorless high dynamic control of a hybrid reluctance machine in the low frequency range including standstill," Ph.D. dissertation, Vienna Univ. Technol., Vienna, Austria, 1998.

[4] T. Wolbank and P. Weinmeier, "The impact of different methods to generate Inform test pulses for sensorless control of a.c. machines on power electronics and the performance of the drive," in *Proc. Int. PCIM*, 1998, vol. 1, pp. 517–523.

[5] J. Holtz and J. Juliet, "Sensorless acquisition of the rotor position angle of induction motors with arbitrary stator windings," *IEEE Trans. Ind. Appl.*, vol. 41, no. 6, pp. 1675–1682, Nov./Dec. 2005.

[6] C. Silva, G. M. Asher, and M. Sumner, "Hybrid rotor position observer for wide speed-range sensorless PM motor drives including zero speed," *IEEE Trans. Ind. Electron.*, vol. 53, no. 2, pp. 373–378, Apr. 2006.

[7] F. Briz, M. Degner, P. Garcia, and A. Diez, "Transient operation of carrier signal injection based sensorless techniques," in *Proc. IEEE IECON*, 2003, vol. 2, pp. 1466–1471.

[8] A. Consoli, "Machine sensorless control techniques based on HF signal injection," in *Proc. EPE-PEMC*, 2000, vol. 1, pp. 98–103.

[9] J. I. Ha and S. K. Sul, "Physical understanding of high frequency injection method to sensorless drives of an induction machine," in *Conf. Rec. IEEE IAS Annu. Meeting*, 2000, pp. 1802–1808.

[10] M. Schroedl, "Sensorless control of AC machines at low speed and standstill based on the inform method," in *Conf. Rec. IEEE IAS Annu. Meeting*, 1996, vol. 1, pp. 270–277.

[11] C. Caruana, G. M. Asher, and J. Claire, "Sensorless vector control at low and zero frequency considering zero-sequence current in delta connected cage induction motors," in *Proc. IEEE IECON*, 2003, pp. 1460–1465.

[12] J. Holtz, "Sensorless position control of induction motors—An emerging technology," in *Proc. IEEE Workshop AMC*, 1998, pp. 1–14.

[13] T. M. Wolbank, J. Machl, and H. Hauser, "Closed-loop compensating sensors versus new current derivative sensors for shaft-sensorless control of inverter fed induction machines," *IEEE Trans. Instrum. Meas.*, vol. 53, no. 4, pp. 1311–1315, Aug. 2004.

[14] N. Bianchi, S. Bolognani, J. Jang, and S. K. Sul, "Comparison of PM motor structures and sensorless control techniques for zero-speed rotor position detection," *IEEE Trans. Power Electron.*, vol. 22, no. 6, pp. 2466–2475, Nov. 2007.

[15] N. Bianchi, S. Bolognani, J. Jang, and S. K. Sul, "Advantages of inset PM machines for zero-speed sensorless position detection," *IEEE Trans. Power Electron.*, vol. 44, no. 6, pp. 1190–1198, Jul./Aug. 2008.

[16] J. Holtz, "Acquisition of position error and magnet polarity for sensorless control of PM synchronous machines," *IEEE Trans. Ind. Appl.*, vol. 4, no. 44, pp. 1172–1180, Jul./Aug. 2008.

[17] R. Pea, R. Cardenas, J. Proboste, G. Asher, and J. Clare, "Sensorless control of doubly-fed induction generators using a rotor-current-based MRAS observer," *IEEE Trans. Ind. Electron.*, vol. 55, no. 1, pp. 330–339, Jan. 2008.

[18] C. Caruana, G. M. Asher, and J. Clare, "Sensorless flux position estimation at low and zero frequency by measuring zero-sequence current in delta-connected cage induction machines," *IEEE Trans. Ind. Appl.*, vol. 41, no. 2, pp. 609–617, Mar./Apr. 2005.
[19] C. S. Staines, G. M. Asher, and M. Sumner, "Rotor-position estimation for induction machines at zero and low frequency utilizing zero-sequence currents," *IEEE Trans. Ind. Appl.*, vol. 42, no. 1, pp. 105–112, Jan./Feb. 2006.
[20] T. Wolbank, M. Vogelsberger, R. Stumberger, S. Mohagheghi, T. Habetler, and R. Harley, "Autonomous self commissioning method for speed sensorless controlled induction machines," in *Conf. Rec. IEEE IAS Annu. Meeting*, 2007, pp. 1179–1185.
[21] T. M. Wolbank, J. Machl, and T. Jaeger, "Combination of signal injection and neural networks for sensorless control of inverter fed induction machines," in *Proc. IEEE PESC*, 2004, pp. 2300–2305.
[22] K. Zimmermann, J. Matas, and T. Svoboda, "Tracking by an optimal sequence of linear predictors," *IEEE Trans. Pattern Anal. Mach. Intell.*, vol. 31, no. 4, pp. 677–692, Apr. 2009.
[23] P. Cortes, M. P. Kazmierkowski, R. M. Kennel, D. E. Quevedo, and J. Rodriguez, "Predictive control in power electronics and drives," *IEEE Trans. Ind. Electron.*, vol. 45, no. 12, pp. 4312–4324, Dec. 2008.
[24] Q. Gao, G. Asher, and M. Sumner, "Sensorless position and speed control of induction motors using high-frequency injection and without offline precommissioning," *IEEE Trans. Ind. Electron.*, vol. 54, no. 5, pp. 2474–2481, Oct. 2007.
[25] A. Consoli, G. Scarcella, G. Scelba, A. Testa, and D. A. Triolo, "Sensorless rotor position estimation in synchronous reluctance motors exploiting a flux deviation approach," *IEEE Trans. Ind. Appl.*, vol. 43, no. 3, pp. 1266–1273, Sep./Oct. 2007.
[26] T. M. Wolbank and M. Metwally, "Speed sensorless flux and position control of induction machines based on pulse injection and multiple saliency extraction," in *Proc. IEEE IECON*, 2008, pp. 1403–1408.
[27] C. A. Hudson, N. S. Lobo, and R. Krishnan, "Sensorless control of single switch-based switched reluctance motor drive using neural network," *IEEE Trans. Ind. Electron.*, vol. 55, no. 1, pp. 321–329, Jan. 2008.
[28] H. A. Toliyat, M. Wlas, and Z. Krzemiriski, "Neural-network-based parameter estimations of induction motors," *IEEE Trans. Ind. Electron.*, vol. 55, no. 4, pp. 1783–1794, Apr. 2008.
[29] J. Mazumdar and R. G. Harley, "Recurrent neural networks trained with backpropagation through time algorithm to estimate nonlinear load harmonic currents," *IEEE Trans. Ind. Electron.*, vol. 55, no. 9, pp. 3484–3491, Sep. 2008.
[30] M. S. Zaky, M. M. Khater, S. S. Shokralla, and H. A. Yasin, "Wide-speed-range estimation with online parameter identification schemes of sensorless induction motor drives," *IEEE Trans. Ind. Electron.*, vol. 56, no. 5, pp. 1699–1707, May 2009.

Markus A. Vogelsberger received the M.S. (with honors) and Ph.D. (with honors) degrees in electrical engineering from Vienna University of Technology, Vienna, Austria, in 2004 and 2009, respectively.

He has been a Scientific Research Assistant in the Department of Electrical Drives and Machines, Vienna University of Technology, since the time he started working toward the Ph.D. degree. His special fields of interest are the transient excitations of induction machines, optimized pulsewidth modulation, and neural-network applications for mechanical sensorless-control strategies.

Stefan Grubic (S'08) received the M.S. degree in electrical engineering from Georgia Institute of Technology, Atlanta, in 2006, and the Dipl.Ing. degree in electrical engineering from the Technische Universität Braunschweig, Braunschweig, Germany, in 2007. He is currently working toward the Ph.D. degree in the School of Electrical and Computer Engineering, Georgia Institute of Technology.

Since January 2007, he has been working, in collaboration with Eaton Corporation, on condition monitoring of electric machines, as a Graduate Research Assistant with the Electric Power Group, Georgia Institute of Technology. His research interests include electric-machine diagnostics, motor drives, power electronics, and the control of electrical machines.

Thomas G. Habetler (S'82–M'83–SM'92–F'02) received the B.S.E.E. and M.S. degrees in electrical engineering from Marquette University, Milwaukee, WI, in 1981 and 1984, respectively, and the Ph.D. degree from the University of Wisconsin, Madison, in 1989.

From 1983 to 1985, he was with the Electro-Motive Division, General Motors, as a Project Engineer. Since 1989, he has been with the Georgia Institute of Technology, Atlanta, where he is currently a Professor of electrical engineering in the School of Electrical and Computer Engineering. His research interests are in electric-machine protection and condition monitoring, as well as drives, and he has published over 200 papers in the field. He is a regular Consultant to industry in the field of condition-based diagnostics for electrical systems.

Dr. Habetler has received four conference prize paper awards from the IEEE Industry Applications Society. He has served on the IEEE Board of Directors as Division II Director. He is the Past President of the IEEE Power Electronics Society and the Past Chair of the Industrial Power Converter Committee of the IEEE Industry Applications Society.

Thomas M. Wolbank (M'99) received the Ph.D. degree in industrial electronics and the Associate Professor degree from Vienna University of Technology, Vienna, Austria, in 1996 and 2004, respectively.

He is currently with the Department of Electrical Drives and Machines, Vienna University of Technology.